Effect of Jet-to-Jet Distance and Pipe Position on Flow and Heat Transfer Features of Active Clearance Control Systems

Lorenzo Cocchi[1]
Department of Industrial Engineering,
University of Florence,
via S. Marta 3,
Florence 50139, Italy
e-mail: lorenzo.cocchi@htc.unifi.it

Alessio Picchi
Department of Industrial Engineering,
University of Florence,
via S. Marta 3,
Florence 50139, Italy
e-mail: alessio.picchi@htc.unifi.it

Bruno Facchini
Department of Industrial Engineering,
University of Florence,
via S. Marta 3,
Florence 50139, Italy
e-mail: bruno.facchini@htc.unifi.it

Riccardo Da Soghe
Ergon Research,
via Campani 50,
Florence 50127, Italy
e-mail: riccardo.dasoghe@ergonresearch.it

Lorenzo Mazzei
Ergon Research,
via Campani 50,
Florence 50127, Italy
e-mail: lorenzo.mazzei@ergonresearch.it

Lorenzo Tarchi
Ergon Research,
via Campani 50,
Florence 50127, Italy
e-mail: lorenzo.tarchi@ergonresearch.it

Laurent Descamps
Safran Aircraft Engines,
Villaroche, Réau 77550, France
e-mail: laurent.descamps@safrangroup.com

Maxime Rotenberg
Safran Aircraft Engines,
Villaroche, Réau 77550, France
e-mail: maxime.rotenberg@safrangroup.com

Effect of Jet-to-Jet Distance and Pipe Position on Flow and Heat Transfer Features of Active Clearance Control Systems

The goal of this work is to investigate the effect of supply pipe position on the heat transfer features of various active clearance control (ACC) geometries, characterized by different jet-to-jet distances. All geometries present 0.8 mm circular impingement holes arranged in a single row. The jets generated by such holes cool a flat target surface, which is replicated by a metal plate in the experimental setup. Measurements are performed using the steady-state technique, obtained by heating up the target plate thanks to an electrically heated Inconel foil applied on the side of the target opposite to the jets. Temperature is also measured on this side by means of an IR camera. Heat transfer is then evaluated thanks to a custom-designed finite difference procedure, capable of solving the inverse conduction problem on the target plate. The effect of pipe positioning is studied in terms of pipe-to-target distance (from 3 to 11 jet diameters) and pipe orientation (i.e., rotation around its axis, from 0 deg to 40 deg with respect to target normal direction), while the investigated jet Reynolds numbers range from 6000 to 10,000. The obtained results reveal that heat transfer is maximized for a given pipe-to-target distance, dependent on both jet-to-jet distance and target surface extension. Pipe rotation also affects the cooling features in a nonmonotonic way, suggesting the existence of different flow regimes related to jet inclination. [DOI: 10.1115/1.4052953]

Introduction

The development of increasingly performing aero engines is mandatory in order to combine the growing expansion of the aviation sector with its environmental sustainability. In particular, an impressive optimization of turbine module efficiency is foreseen in order to reach the goals set by ACARE Flightpath 2050 strategy [1]. In this framework, a key role can be played by the control of tip leakages of high- and low-pressure turbines: in fact, the flows evolving through the outer ring cavities and the labyrinth seals do not contribute to the power generation and can also interact with the main flow, thus inducing mixing losses and further deteriorating efficiency. This situation is worsened by the strongly variable operating conditions experienced by the engine during its mission since centrifugal and thermal loads can significantly alter the clearances between rotating and stationary components. In order to mitigate this phenomenon, active clearance control (ACC) systems were introduced with the aim to optimize the clearances along with the various phases of the engine mission. This is achieved by managing the thermal deformations of the turbine casing: to do so, a series of circumferential supply pipes embrace the casing, and cooling air jets are generated by perforations on the inner side of such pipes. An example of low pressure turbine ACC (LPTACC) system is presented in Fig. 1.

Jet impingement has been widely applied and studied in the turbomachinery framework for since decades (extensive reviews can be found in Refs. [2–4]). Even so, the typical features of ACC systems make their flow and heat transfer features significantly different from the ones traditionally associated with impinging jets. In fact, in ACC devices a very large number of jets are usually

[1]Corresponding author.

Manuscript received September 28, 2021; final manuscript received October 11, 2021; published online January 21, 2022. Editor: Jerzy T. Sawicki.

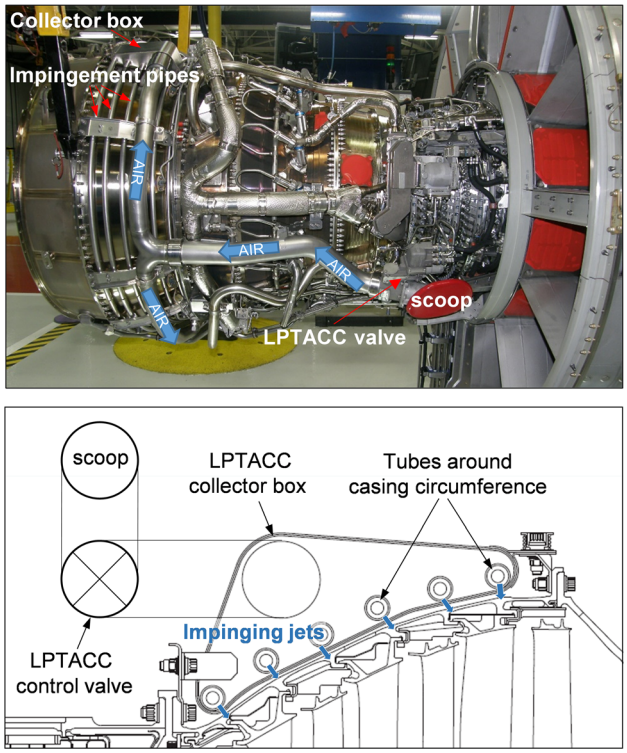

Fig. 1 CFM56-5B LPTACC system (up), LPTACC functional sketch (down)—Safran Aircraft Engines

generated by a relatively long manifold: this can create a relevant crossflow upstream of the jets, whose magnitude also varies along the manifold itself. As a result, the mass flow split amongst the impingement holes can be affected, due to the locally different discharge coefficients for the single holes. Interesting contributions on this topic come from Da Soghe and Andreini [5,6]: basing on LPTACC real engine arrangements, a correlation was obtained for the discharge coefficient of every single hole in a wide range of operating conditions in terms of jet Reynolds number and pressure ratio. Considering target plate heat transfer, only a small number of works deals with jets arranged in one or more rows. In this sense, one of the first relevant investigations is given by Goldstein and Seol [7], who expressed heat transfer as a function of Re and of the geometrical parameters for a single row of impinging jets, also retrieving a correlation for line averaged Nusselt number Nu.

More recently, interesting contributions were provided by a series of works explicitly focusing on ACC systems, like the ones of Ben Ahmed et al. [8–10] and of Merzec and Kucabba-Pietal [11]: all of these works investigated discharge coefficients and heat transfer values for a section of an LPTACC system, also considering the effect of different hole shapes. The outer casing surface can also house ribs, which alter the target surface shape for ACC systems. This typically occurs in the high-pressure turbine section and was studied by Choi et al. [12] and Liu et al. [13,14]. On the other hand, as low-pressure turbine ACC is concerned, a transverse flow in the undercowl cavity may occur, which can significantly affect the heat transfer for the upstream rails [15]. Another typical feature of ACC systems is that, due to the length of the supply pipes and to their vicinity with the hot turbine casing, the cooling flow may heat up inside the pipes, reducing the cooling potential [16]. This situation is worsened by the fact that coolant extraction may enhance the heat transfer inside the supply pipe [17].

This brief literature review revealed that the performance of an ACC system can be affected by a large number of characteristic phenomena. As a consequence, during the design phase the choice of the geometric features of the system may not be driven only by the classic rules retrieved from the study of a single jet, but needs to consider the specific features of ACC devices. This is demonstrated by the fact that the correlations usually employed to retrieve jet impingement heat transfer often fail when applied to an ACC system [8,14]. Moreover, in this case, the size of the system (i.e., the length of the pipe) is at least two orders of magnitude larger than the size of the local geometry (i.e., hole diameter and pipe-to-target distance). As a consequence, small mounting tolerances or thermal displacements may result in a relevant alteration of the local cooling geometry, mainly in terms of pipe-to-target distance and pipe rotation around its axis. Both of these phenomena deserve a thorough investigation. In fact, the effect of jet-to-target distance might be different for a row of jets with respect to a single one [7]. On the other hand, while many works investigated the effect of a single oblique jet [18–20], to the authors' knowledge no contribution exists regarding a row of inclined jets.

Based on these considerations, the goal of this work is to study the effect of pipe position on the cooling performance of different ACC geometries, with the aim to provide valuable indications regarding both the design of ACC systems and their sensitivity to mounting tolerances and thermal deformations. In order to achieve the best similarity with the real system, the investigation is carried out by means of experimental analysis, using real scale, fully metallic test samples, and target surfaces. To reach this goal, the experimental configuration and data postprocessing technique already validated in previous work by the same authors [21] has been employed.

Experimental Setup

Investigated Geometries and Conditions. The system investigated in this work replicates a sector of an LPTACC system. Given the large curvature radius of the turbine casing with respect to the system features, the casing outer surface is modeled as a flat plate and the ACC manifold as straight. In particular, the manifold consists of a circular pipe, housing a single row of round holes on the side facing the plate. The manifold has an outer diameter D of 19.05 mm and a thickness t of 0.71 mm, while impingement holes diameter d is 0.8 mm. The length of the test section is 200 mm, and the manifold is closed at the end: as a consequence, the only internal crossflow for the impingement holes will be given by the flow feeding the holes themselves. A scheme of the investigated system and of the relevant geometric parameters is presented in Fig. 2(*a*).

In order to retrieve a complete comprehension of the pipe positioning effect, three different impingement geometries were considered, with different values of jet-to-jet distance Y. In particular,

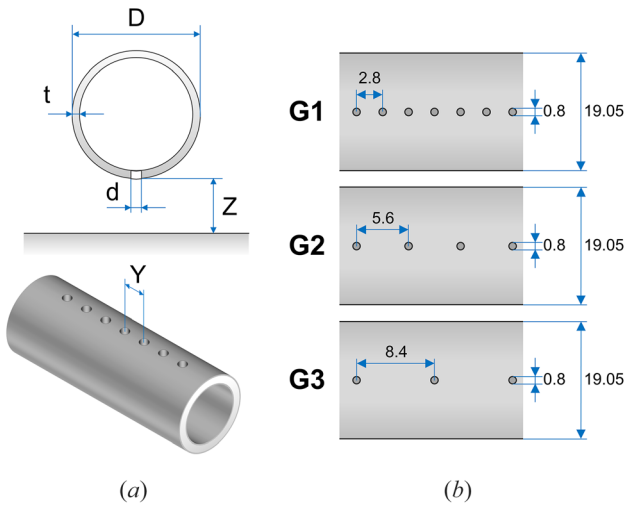

Fig. 2 (*a*) Cooling system and (*b*) investigated geometries

for the densest hole pattern (denoted as G1) Y is equal to 3.5 diameters, while for the other geometries (denoted as G2 and G3) this value is two and three times, respectively. These values were selected to cover a significant range of hole densities for ACC geometries, spanning from very dense to very sparse. The features of these geometries are presented in Fig. 2(*b*) and summarized in Table 1.

Flow conditions were specified by the value of the overall jet Reynolds number, defined as

$$\mathrm{Re} = \frac{\mathrm{md}}{A_{\mathrm{tot}}\mu} \tag{1}$$

where m is the total mass flow rate, A_{tot} is the overall passage area for all the impingement holes and μ is the flow dynamic viscosity, evaluated at the jet total temperature.

The effect of pipe positioning was considered in terms of both pipe-to-target distance and pipe orientation. In particular, five different values of pipe-to-target distance Z were investigated, spanning from 3 to 11 jet diameters. On the other hand, pipe orientation was identified by the pipe rotation angle around its axis, denoted as α. Six values of α were studied, ranging from 0 deg to 40 deg, with $\alpha = 0$ deg corresponding to the orientation where the impingement holes axes are perpendicular to the target. In order to limit the experimental effort, pipe rotation is only investigated for Z/d equal to 3, 7, and 11 and for a fixed Re of 8000.

Experimental Apparatus. The heat transfer features of the aforementioned geometries were investigated thanks to a suitable experimental apparatus, installed in the Heat Transfer and Combustion Laboratory of the Department of Industrial Engineering of the University of Florence.

In order to reliably replicate the actual features of a real ACC system, the same material and manufacturing techniques were employed in the realization of the test samples. In particular, the manifold is made of an 800 mm long stainless steel pipe, and impingement holes were realized via electrical discharge machining. This choice allows to replicate the local geometric features induced by the manufacturing, thus including their effect in the investigation: in fact, local hole geometry can significantly affect the flow and heat transfer characteristics of the system [9]. Since the jet-to-jet distances of geometries G2 and G3 are multiple of the value for geometry G1, a single test sample was realized replicating the latter configuration, and geometries G2 and G3 were obtained by plugging the required number of holes by means of leakage proof tape.

The samples were tested using a suitable test rig (a scheme of which is reported in Fig. 3), developed in order to test ACC geometries up to 400 mm long. The rig is fed by compressed air, which is supplied by a system capable of providing up to 45 g/s of dry air at 7 bar. A filtering section and a pressure regulator were installed downstream such system, in order to supply the rig with a pure flow at constant pressure, while a shutter valve allows mass flow regulation.

The main component of the rig is the test section, which actually replicates the cooling geometry. The test section, a

Table 1 Features of the investigated geometries

Geometry		G1	G2	G3
Hole diameter	d (mm)	0.80	0.80	0.80
Jet-to-jet distance	Y (mm)	2.80	5.60	8.40
	Y/d	3.5	7.0	10.5
ACC pipe thickness	t (mm)	0.71	0.71	0.71
	t/d	0.89	0.89	0.89
ACC pipe diameter	D (mm)	19.05	19.05	19.05
Number of holes	N	72	36	24

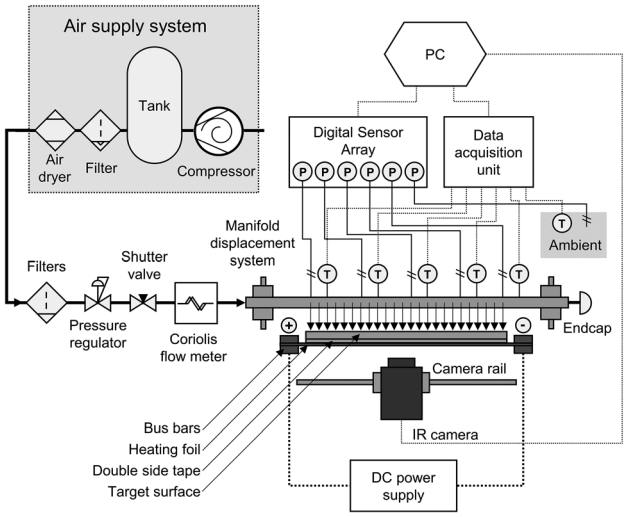

Fig. 3 Scheme of the test rig

picture of which is presented in Fig. 4, is made of a stainless steel frame, which hosts both the ACC manifold and the jet target plate and allows to set a rigid relative positioning for these components. In particular, the target plate is replicated by a horizontal 0.4 mm thick Inconel X750 plate, 400 mm long and 80 mm wide, provided by ILT Tecnologie (Ponsacco, PI, Italy).

The test rig allows to measure heat transfer by using the steady-state technique. In order to apply such a method, constant heat flux is applied to the target thanks to an electrically heated Inconel foil (25.4 μm thick), fed by a direct current power supply (Agilent N5763A) via a pair of copper bus bars. The heating foil is applied to the target on the opposite side of the jets using high temperature-resistant double-sided tape (0.2 mm thick).

While the jet target surface is fixed, the ACC manifold can be displaced thanks to two rotary stages (Thorlabs XYR1/M), capable of $\pm$12.5 mm displacement in both orthogonal directions (0.01 mm accuracy) as well as of 360 deg rotation (1 deg accuracy). To obtain a rigid connection between the manifold and the rotary stages custom designed stainless steel clamps were employed, housing a centering pin that fits in a corresponding hole of the manifold.

The temperature of the target surface was sampled by means of a FLIR SC6700 IR camera, installed on a sliding rail in order to quickly displace it in different locations and obtain a full view of the target plate. In particular, the temperature was measured on the target external surface, i.e., the one opposite to the ACC manifold: in fact, a direct measurement on the inner surface is difficult to obtain, given the low pipe-to-target distance and the presence of the pipe itself. To improve the measurement accuracy, the surface was covered with a thin layer of high temperature, high

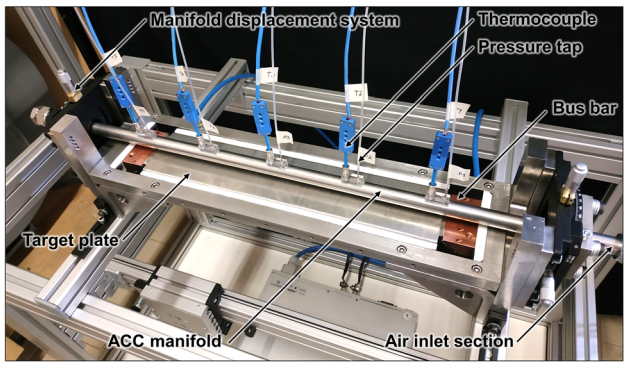

Fig. 4 Picture of the test section

emissivity black paint. The employed paint was selected based on the quality of the surface finish: since the postprocessing technique described in the Data Postprocessing section is based on the solution of an inverse heat conduction problem, measurement noise shall be reduced as much as possible, and thus paints providing a grainy finish shall be avoided. The emissivity of the paint was calibrated thanks to a dedicated apparatus, consisting of a flat aluminum sample, painted on one side and heated on the opposite one by means of a film heater of the same size. All sides but the painted one are enclosed in insulating foam. Emissivity values were retrieved by observing the painted side with the IR camera and targeting its reading with the measurement of a thermocouple embedded in the sample. It was found that emissivity is insensitive to the viewing angle in the investigated range, while a slight dependency on the temperature was recorded and thus employed to correct the camera readings.

Apart from the temperature of the target, other values are required to determine the heat transfer features. In particular, the jet total temperature was sampled on the centerline of the pipe in five axial locations, equally spaced along the pipe drilled section: this allows to rebuild the flow temperature distribution along the pipe, thus taking into account the possible effect of ACC manifold heating due to convection and radiation [16]. Ambient temperature was also sampled on both sides of the target in order to evaluate the heat losses. All temperatures were measured with type T thermocouples (0.5 K relative accuracy), connected to a data acquisition unit (Agilent 34970A), and a temperature-controlled cold junction (Pt100, 0.1 K absolute accuracy).

Static pressure was also sampled in the same locations of the thermocouples using a Scanivalve DSA 3217 scanner (15 Pa accuracy), while inlet mass flow rate was provided by a Coriolis flowmeter (Bronkhorst CORI-FLOW^{TM} M55, 12 g/s range, 0.5% accuracy.

Data Postprocessing. In this work, the experimental procedure and postprocessing technique presented and validated in a previous work of the same authors [21] was employed to retrieve heat transfer data: as a consequence, only a brief recap will be presented in the following.

Dedicated tests were carried out in order to retrieve the distribution of convective heat transfer coefficient h on the jet target surface, which is defined as

$$h = \frac{q_{\text{conv,int}}}{T_w - T_{\text{ad},w}} \tag{2}$$

where $q_{\text{conv,int}}$ is the convective heat flux on the impingement side of the target plate, T_w is the corresponding wall temperature and $T_{\text{ad},w}$ is the adiabatic wall temperature. The use of $T_{\text{ad},w}$ as reference flow temperature for the definition of h is a common choice in the open literature, since using this definition h is independent of the value of the wall heat flux [22]. Recovery effects can lead the adiabatic wall temperature $T_{\text{ad},w}$ to be significantly different from the jet total temperature $T_{0,j}$. When the jet velocity is low the dynamic temperature is also small, thus the aforementioned difference can usually be neglected [23]. However, the flow conditions investigated in this work correspond to jet velocities approaching 200 m/s for the largest Re value, thus a proper evaluation of the recovery effects is required. To achieve this goal, the linear regression method was employed [24,25]. In this case, two tests were performed in each investigated condition: a "hot" test and a "cold" test. In the "hot" test, to minimize measurement uncertainty the thermal power was set to the maximum allowable value, corresponding to the one providing a target temperature lower than the thermal resistance of the double-side tape (around 100 °C) in every point. In the "cold" test, the minimum thermal power level was imposed, corresponding to temperature gradients along with the plate sufficiently larger than the temperature measurement uncertainty. Zero heat flux temperature (i.e., adiabatic wall temperature) was then evaluated by means of the linear regression between wall heat flux and wall temperature values of the two tests, while the slope of the regression provides h. The low thermal power test, in particular, allows to perform regression with a point in nearly adiabatic conditions, thus reducing the extrapolation of the linear fitting required to find $T_{\text{ad},w}$ and increasing the measurement robustness. During these tests, it was verified that the difference between jet total temperature and ambient temperature was within 0.1 K, thus avoiding spurious effects related to flow entrainment [7]. As an example, Fig. 5(*a*) presents regression lines for two points located on the jet stagnation line ($x/d = 0$) and 10 diameters away ($x/d = 10$) obtained with geometry G1. Heat flux is plotted as a function of the difference between wall and jet total (, i.e., ambient) temperature $T_{0,j}$ to take into account slight alterations of the latter parameter between the two tests. As expected, close to the jet stagnation a larger slope occurs (i.e., a larger h value) and the regression line crosses the horizontal axis at a positive value (i.e., the adiabatic wall temperature is higher than the jet one). In fact, due to the large flow velocity the jet static temperature decreases and becomes significantly lower than the ambient one: the entrainment of ambient air will thus result in an increase of jet temperature, eventually leading to a hotter-than-ambient recovery temperature [7]. On the other hand, far from the jet stagnation, the fit crosses the horizontal axis close to zero, suggesting negligible recovery phenomena in this region. These behaviors are also shown by the $T_{\text{ad},w}$ distribution presented in Fig. 5(*b*).

In order to evaluate h on the inner side of the target, the values of wall temperature and heat flux need to be known. Since in this case temperature measurement is performed on the outer side of the target, to retrieve these values an inverse heat conduction problem within the target needs to be solved. This is performed by applying a finite difference explicit procedure developed by the same authors [21], implemented in MATLAB, which will be briefly presented in the following.

The first operation performed by the postprocessing procedure is the discretization of the target surface. A square mesh is built on the outer side of the target (i.e., where the temperature is measured), and a node is placed in the geometric center of every element. The thickness of the target is then also discretized: every layer is divided into one or more sublayers, and the outer surface mesh is extruded toward the inner side to define volume elements. A node is placed halfway to the thickness of each sublayer as well as on the inner surface. As reported in Fig. 6, in the present case, every layer was discretized as a single layer, while a grid sizing of 0.2 mm is employed on the outer surface, approximately corresponding to the camera resolution.

For every element of the outer surface, the dispersed heat fluxes are then evaluated as

$$q_{\text{conv,ext}} = h_{\text{ext}}(T_{\text{ext}} - T_{\text{amb}}) \tag{3}$$

$$q_{\text{rad,ext}} = \sigma\varepsilon\,(T_{\text{ext}}^4 - T_{\text{amb}}^4) \tag{4}$$

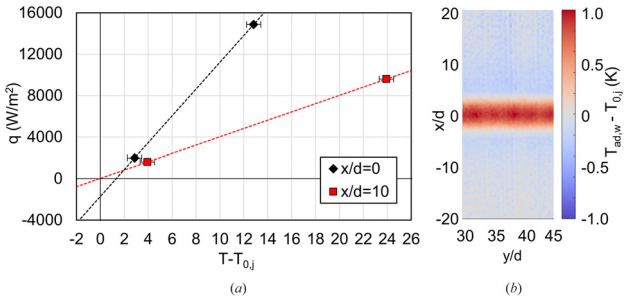

Fig. 5 (*a*) sample regression plots and (*b*) adiabatic wall temperature distribution—G1 geometry, Re = 10,000, *Z/d* = 11

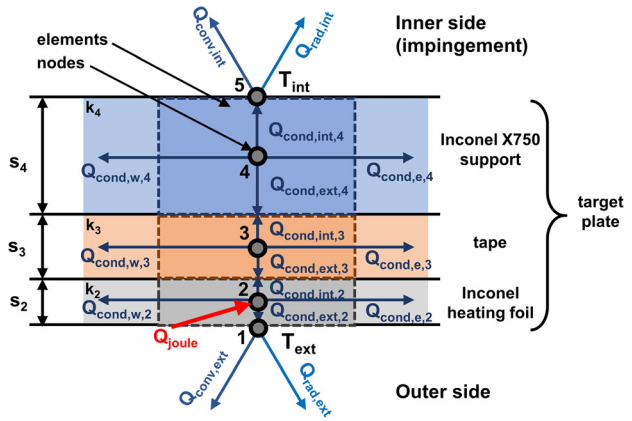

Fig. 6 Target plate discretization

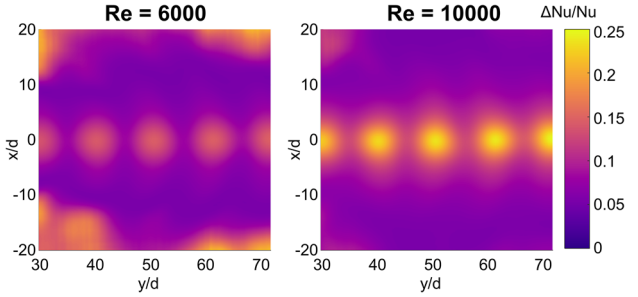

Fig. 7 Sample Nu uncertainty distributions—G3 geometry, *Z/d* = 3

where h_{ext} is the external convective heat transfer coefficient (obtained from literature correlations [26] in this case), σ is the Stefan-Boltzmann constant, ε is the external surface emissivity (i.e., paint emissivity), T_{amb} is the ambient temperature and T_{ext} is the external node temperature.

Applying energy balance to the outer node, the sum of $q_{conv,ext}$, and $q_{rad,ext}$ equals the conductive flux $q_{cond,ext,2}$ from the first inner node (node 2 in Fig. 6) to the outer one (node 1): since the temperature of the outer node is known, solving the conduction equation will provide the temperature of the first internal node. Generalizing this procedure for a generic layer, the element nodal temperature if an ith layer can be obtained from the nodal temperature of the outer element T_{i-1} solving

$$T_i = T_{i-1} + R_{ext,i} \cdot q_{cond,ext,i} \tag{5}$$

where R_{ext} is the external conductive resistance. If this is repeated for every point of the outer surface, the internal temperature distribution of the first sublayer is obtained, which allows to estimate the side heat fluxes occurring in between the elements of the sublayer. As an example, the heat flux toward the northern element is

$$q_{cond,n,i} = \frac{1}{R_{n,i}}(T_i - T_{n,i}) \tag{6}$$

where $R_{n,i}$ is the resistance between adjacent elements.

One of the main issues of inverse heat conduction problems is that they are generally ill-posed [27]: as a consequence, small variations in the input data may result in a strong alteration of the obtained results. On the one hand, this requires that the quality of the input data is as good as possible (hence the requirements on paint selection). On the other hand, some regularization is needed to limit the solution drift toward unrealistic patterns. The most critical aspect for this procedure consists in the evaluation of lateral heat fluxes: in fact, temperature noise of interpolation issue may produce unphysical values for the temperature difference in the right-hand side of Eq. (6), which then get amplified in the evaluation of q_{cond} by the low value of the local thermal resistance. In order to solve this issue, the developed procedure smooths down the side heat fluxes patterns, i.e., the matrices representing their values for every layer. Any smoothing filter with a circular kernel is suitable for this purpose: in fact, if the thermal properties of the layer material are isotropic a direction-independent smoothing shall be applied. The size of the kernel shall be defined from a sensitivity analysis as a tradeoff between the noise removal capability and the preservation of the heat transfer pattern detail. In this case, side heat fluxes were smoothed using a moving average, based on a circular kernel with a 1 mm radius.

Once all of the heat fluxes are known for a single element, the heat flux $Q_{cond,int}$ toward the inner surface can be evaluated for a given element by imposing energy balance

$$Q_{cond,ext,i} + Q_{cond,n,i} + Q_{cond,s,i} + Q_{cond,e,i} + Q_{cond,w,i} + Q_{cond,int,i} - Q_{gen,i} = 0 \tag{7}$$

where the single terms are obtained by multiplying the specific heat fluxes per the corresponding element face area. The term $Q_{gen,i}$ takes into account internal heat generation, if present. Since $Q_{cond,int,i}$ is equal to $Q_{cond,ext,i+1}$, Eq. (5) will thus provide the temperature of the following sublayer.

All of the aforementioned operations are repeated for every sublayer until the inner surface is reached. The procedure thus directly provides the temperature distribution on this surface, while convective heat flux $q_{conv,int}$ can be obtained by subtracting the radiative heat flux $q_{rad,int}$ from $q_{cond,int}$. Once this is done, the inner h value can be evaluated using Eq. (2). For the present case, the whole procedure takes around 5 s to run.

Local h values can be reformulated in a dimensionless form as Nusselt number values

$$Nu = \frac{hd}{k} \tag{8}$$

where k is air thermal conductivity evaluated at local film temperature.

Measurement Uncertainty. Given the complexity of the post-processing procedure presented in the section Data Postprocessing, a Monte Carlo approach [28] was employed to retrieve the uncertainty associated with Nu values. In particular, the procedure was repeated multiple times and for each repetition, every input was randomly varied within its statistical uncertainty distribution. Local uncertainty of the output (i.e., Nu) can thus be evaluated based on the corresponding dispersion in every point. In the present case, a 95% confidence level was considered to retrieve local uncertainty. The number of procedure repetitions required for the method to converge (i.e., the uncertainty values are not affected by additional repetitions) is around 5000.

For the present case, the largest uncertainty was retrieved for the lowest investigated pipe-to-target distance, since in this case, the strongest temperature gradients along the target plate occur. Figure 7 presents sample Nu uncertainty distributions obtained in this condition with the sparsest hole geometry, for both the smallest and the largest Re values. If the jet stagnation region is considered (i.e., close to $x/d = 0$) the maximum uncertainty is obtained for the largest Re: in fact, in this condition the lowest wall temperature occurs in this zone, and thus local uncertainty is strongly affected by the accuracy of temperature measurement. On the other hand, if the regions far from jet stagnation are considered, the largest uncertainty is found for the lowest Re, since the low

heat transfer values make the contribution of the uncertainty on the dispersed heat fluxes relevant. In every case, uncertainties on Nu area-averaged values range from 8% to 11%.

Uncertainty on Reynolds number was evaluated according to the standard ANSI/ASME PTC 19.1 [29] based on Kline and McClintock method [30]. Maximum uncertainty is equal to 2.51%, corresponding to the smallest mass flow rate, i.e., to the lowest Re with the sparsest hole geometry (G3).

Results

In this section, the outcomes of the experimental campaign will be presented as Nu distributions on the jet target surface. Unless otherwise specified, the results presented in this section were obtained with impingement jets perpendicular to the target ($\alpha = 0$ deg).

Effect of Jet-to-Jet Spacing. Before discussing the effect of the actual pipe positioning on heat transfer, it is worth highlighting the differences between the three investigated geometries, in order to provide a clearer frame for the interpretation of the single effects. Sample two-dimensional (2D) Nu distributions obtained for the intermediate Re and Z/d values are presented in Fig. 8. The coordinate y (streamwise) is aligned with the ACC pipe axis while the coordinate x (spanwise) identifies the perpendicular direction; $y = 0$ corresponds to the leftmost edge of the target, while $x = 0$ is set on the jet stagnation line. Coolant is fed from the right side of the maps. A single heat transfer peak is present for every jet, aligned with the corresponding hole. Heat transfer shape and magnitude seem slightly different in between the peaks: this can be interpreted as the effect of the manufacturing, which may induce small differences in the real hole geometry. Even so, local differences in peak magnitude fit within ±6.5% of the average peak value. Heat transfer monotonically decreases moving away from the stagnation line: in this region, wake-like elongations of the Nu distribution are present in the streamwise direction on both sides of every jet. These structures can be attributed to the shape of the wall jet induced by flow confinement, which makes the spent coolant leave the stagnation zone mainly in the spanwise direction.

Even if a crossflow is present upstream of the impingement holes, this seems to have very little effect on the heat transfer peaks: in fact, no clear trend can be identified in the supply flow direction (i.e., moving toward the negative y direction). This effect was somewhat expected, given the large jet velocity with respect to the supply flow one (mass velocity ratio is larger than 5 in every condition [5]). On the other hand, for the sparsest hole pattern (G3) some crossflow effect seems to occur on the wall jet, since the aforementioned elongated Nu structures appear to be slightly bent toward the left, i.e., in the supply flow direction.

Figure 8 also suggests that local heat transfer values are weakly affected by jet-to-jet distance, and that differences between the three cases only occur in those regions where local geometry is different (i.e., where no holes are present for the sparser patterns). This is highlighted by Fig. 9, where local Nu values are sampled in the same locations for the three geometries, i.e., along the stagnation line and on a streamwise direction passing through a peak. It can be noticed that peak magnitude is always similar and that values are also very close in those regions where the three hole patterns share the same local geometry. This seems to suggest that the heat transfer pattern is self-similar in the investigated arrangement: even if this is not within the scope of this work, this feature might be very handy in order to define a correlative approach for the prediction of cooling performance, since the whole heat transfer distribution might be rebuilt by combining sections of a "sample" distribution according to jet-to-jet distance.

This local similarity also suggests that in the present case jet-jet interaction is limited, which is verified even for large jet-to-target plate distances ($Z/d = 11$) and dense patterns (G1).

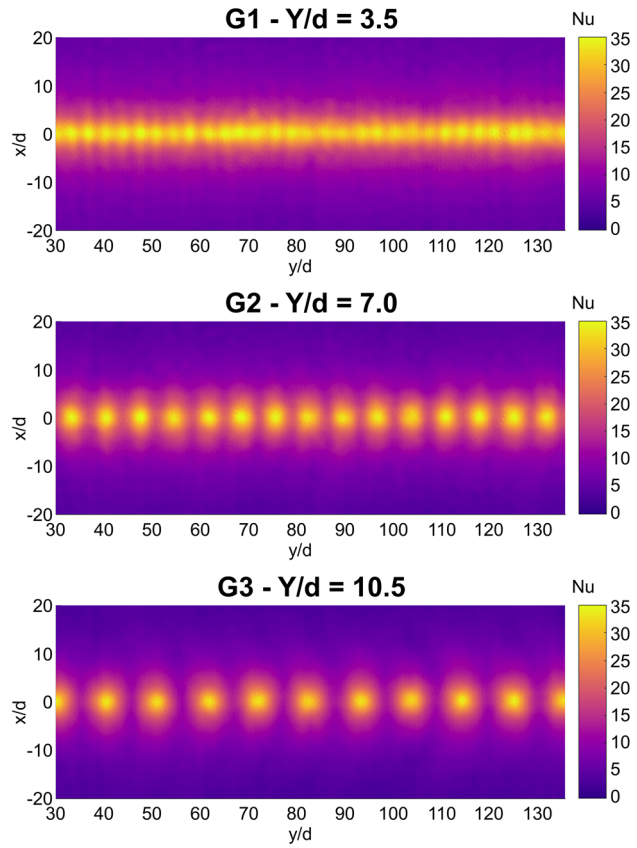

Fig. 8 2D Nu distributions for the three geometries—Re = 8000, $Z/d = 7$

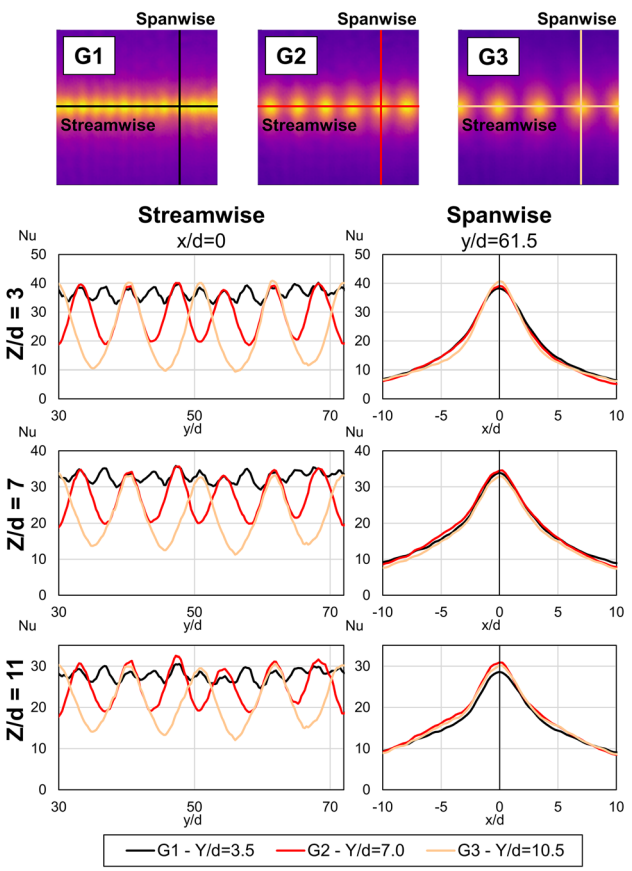

Fig. 9 Local Nu values for the three geometries—Re = 8000

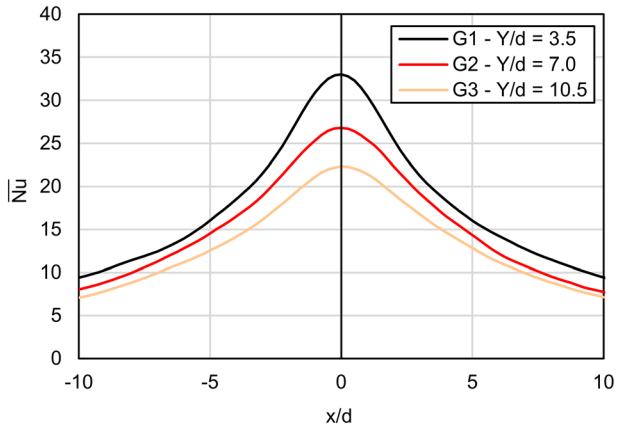

Fig. 10 Line averaged Nu distributions for the three geometries—Re = 8000, *Z/d* = 7

In order to provide a quantitative comparison between the geometries, in Fig. 10 the spanwise distributions of line averaged Nu for the three hole patterns are presented, obtained by averaging the 2D maps over a whole number of jets in the streamwise direction. As expected, heat transfer monotonically increases as jet-to-jet distance decreases, i.e., as mass flow addition increases. Even so, considering that G1 draws three times the coolant mass flow rate of G3, it is evident that heat transfer performance is not proportional to this parameter and that the sparsest geometry is the most effective in terms of coolant consumption.

If different test conditions are considered (not shown for the sake of brevity) the relative difference between the three geometries decreases as both Re and Z/d increase.

Effect of Pipe-to-Target Spacing. For an ACC manifold with a single row of impingement holes perpendicular to the target surface, the relative distance Z between the pipe and the target also corresponds to the actual jet-to-target plate distance. The effect of such parameter on the shape of the heat transfer pattern can be retrieved from Fig. 11, where sample 2D Nu distributions obtained for different Z/d values are reported.

For low Z/d values, the distributions present intense Nu peaks: for the densest hole pattern (G1) such peaks appear very close to the one with the others, while as jet-to-jet spacing increases strong minima occur in between each couple of adjacent jets (see geometry G3). This latter phenomenon seems coherent with a strong jet confinement effect, directly related to the proximity of the supply pipe to the target. In every case, the heat transfer quickly drops moving away from the stagnation region. As Z/d increases, the magnitude of heat transfer peaks decreases, while local Nu values increase in all the surrounding zones, eventually resulting in a smoother and more uniform heat transfer pattern: in other words, the effect of pipe-to-target distance seems to be local. This phenomenon can be attributed to shear effects redistributing the jet momentum over a wider region as Z/d increases, decreasing the jet peak velocity and widening the velocity profile [4].

Pipe-to-target distance also seems to affect the shape of the wall jet: in fact, while for low Z/d the elongations surrounding heat transfer peaks are bent in the supply flow direction (i.e., toward the left side of the map), for large Z/d such structures are perpendicular to the pipe. This is evident in particular for the sparsest hole pattern (G3), while as jet-to-jet spacing decreases the single elongations become more difficult to identify.

The aforementioned local phenomena have a direct effect on line and area-averaged values. This can be appreciated looking at Fig. 12, where the spanwise distributions of line averaged Nu obtained for the three geometries are presented. In every case, as Z/d increases, heat transfer decreases close to jet stagnation and increases in the surrounding regions. Even so, the magnitude and extent of such phenomenon depend upon the geometry, i.e., upon jet-to-jet distance: as Z/d increases, the Nu decrease close to the jet stagnation is more intense as Y/d decreases, while the increase in the surrounding regions is stronger for larger Y/d values. In every case, all the distributions also seem to cross in a single region, which however draws closer to the jet stagnation as Y/d increases (i.e., moving from G1 to G3). All of these phenomena can be justified considering the suppositions derived from 2D Nu distributions: for the densest hole pattern, most of the points close to the stagnation line ($x = 0$) fall within the region where an increase of Z/d is detrimental for heat transfer, thus also affecting the line averaged values; on the other hand, for the sparsest hole pattern even in between the jets significant regions are present which are positively affected by an increase in Z/d (as shown in Fig. 11), thus partly compensating the heat transfer decrease.

Area averaged Nu values can be obtained by averaging local values over a region including a whole number of jets in the streamwise direction, while different extensions in the spanwise direction can be considered starting from the stagnation line. The spanwise extension of the averaging region affects not only the obtained values but also the behavior with respect to pipe-to-target distance, as shown in Fig. 13 for G2 geometry. If such extension is reduced to zero, line averaged values along the stagnation line are obtained, presented in the upper left chart of Fig. 13. The trend reflects the outcomes already obtained from Fig. 12: at jet stagnation, Nu monotonically decreases as Z increases. This phenomenon seems to suggest that, for the present case, the length of the jet potential core is shorter than the minimum investigated Z/d value since for impinging jets a maximum in stagnation heat transfer usually occurs when jet-to-target distance is equal to the length of the potential core [31]. While for a single jet such distance is equal to 4–8 diameters [4], lower values are likely to occur when a multiple jet arrangement is considered [7]. On the other hand, if the extension of the averaging region is increased a local maximum starts to become visible in the trends. The Z/d value corresponding to such maximum seems weakly dependent on Reynolds number, while a clear relation seems to be

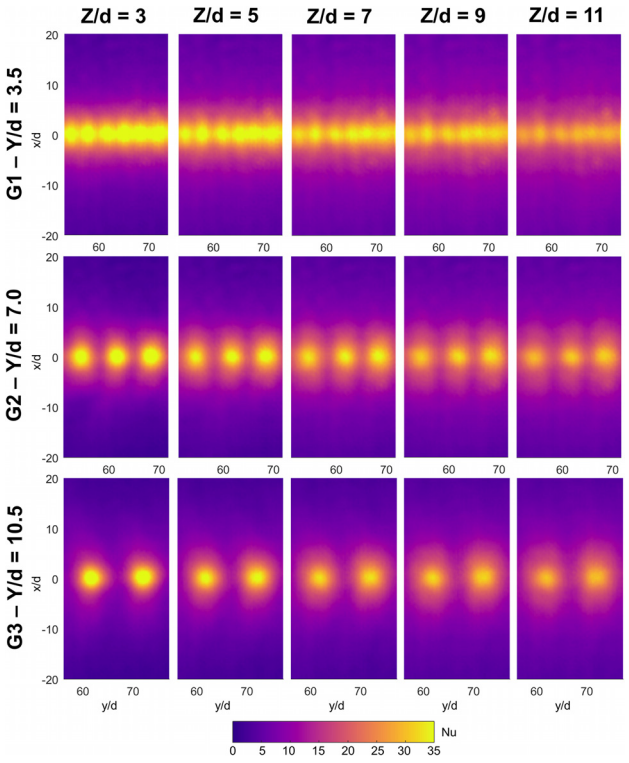

Fig. 11 *Z/d* effect on 2D Nu distributions for the three geometries—Re = 8000

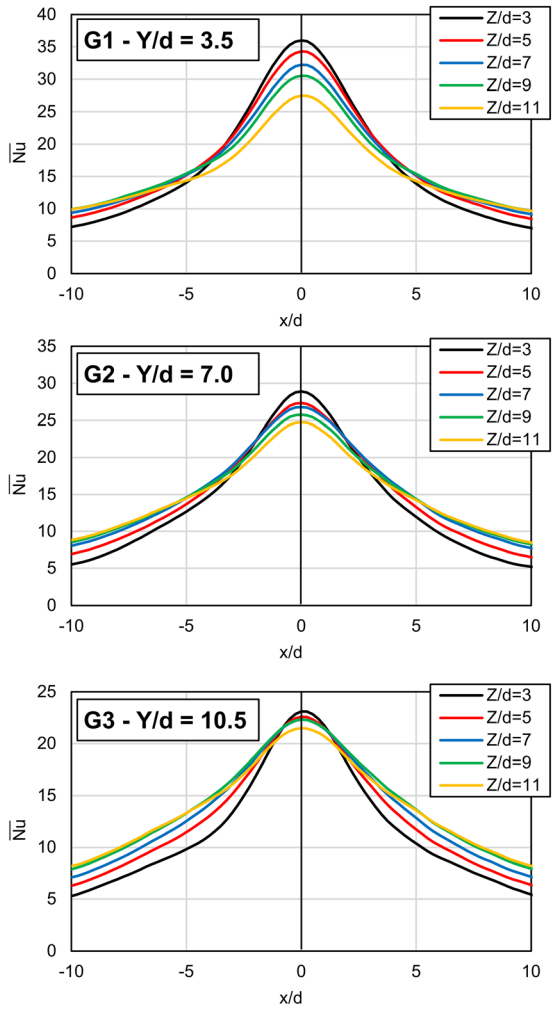

Fig. 12 *Z/d* effect on line averaged Nu distributions—Re = 8000

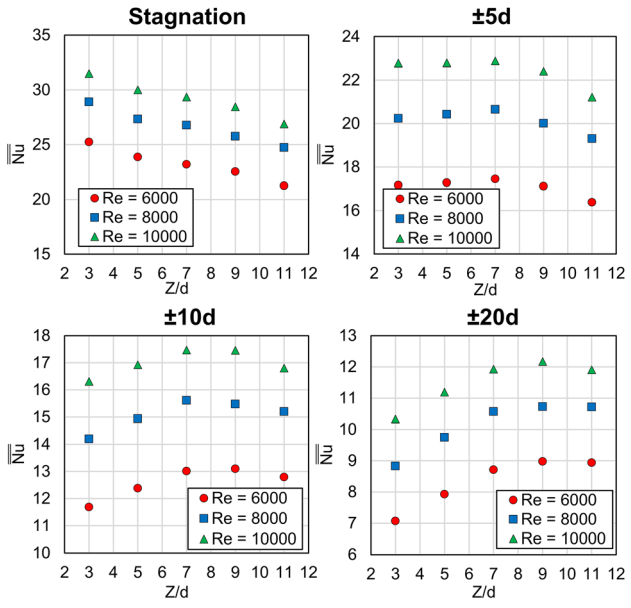

Fig. 13 Area-averaged Nu values as a function of *Z/d* for different extensions of the averaging region—G2 geometry

present with the width of the averaging region: as the spanwise extension moves from $\pm 5d$ to $\pm 20d$ the maximum shifts toward larger Z/d values. In other words, the optimum value of pipe-to-target distance (i.e., the one maximizing heat transfer) depends on the width of the region to be cooled.

The optimum Z/d value seems also affected by the density of the hole pattern: as shown by Fig. 14(a), the maximum heat transfer occurs for larger Z/d values as jet-to-jet distance increases, i.e., moving from geometry G1 to G3.

To provide a clearer visualization of these phenomena, in Fig. 14(*b*) the optimum Z/d value is reported as a function of the spanwise extension of the averaging area for the three investigated geometries. In order to retrieve the optimum Z/d from the discrete investigated values, Nu versus Z/d trends was interpolated with a third-degree polynomial fitting. For all the curves, below a certain extension, the maximum is found for $Z/d = 3$, since this is the lowest investigated value of this parameter and no extrapolation was performed. Beyond such value, the optimum is found for progressively larger Z/d values, with a trend that is almost asymptotic in shape. Taking into account the three geometries, the chart clearly shows that the optimum Z/d value grows with both jet-to-jet distance and with the extension of the area to be cooled: as a consequence, both these parameters shall be taken into account for the definition of pipe stand distance in the design of an ACC system.

Effect of Jet Reynolds Number. Some interesting insight on the system behavior can also be retrieved if the effect of jet Reynolds number is considered. Figure 15 presents the area-averaged values in the region within $\pm 10d$ from the stagnation line for the three geometries. As expected, in every case the average Nusselt values increase with jet Reynolds number, with the relation closely following an exponential trend: as so, for each configuration a fitting in the form $\mathrm{Nu} = a \cdot \mathrm{Re}^b$ was retrieved. If a single geometry is taken into account, it can be noticed that the exponent of Re tends to decrease as pipe-to-target distance Z increases. Since lower values of the Re exponent are associated with a laminar flow, Fig. 15 suggests that an increasingly laminar flow field occurs as the pipe is moved away from the target. An explanation of this phenomenon could be provided by considering that, if jet-to-target distance increases, the jet itself is expected to be wider and more spread when reaching the solid surface: as a consequence, a wider region of the target will experience a directly impinging flow (i.e., direct mass addition) for the wall jet developing along the surface. Such mass flow addition will generate an accelerating wall jet, which in turn may promote a mostly laminar flow close to the target surface. The extension of the target experiencing a laminar wall jet will thus increase with jet-to-target distance, hence the decrease in Re exponent. In the present case, the laminar behavior could be further emphasized by the investigated

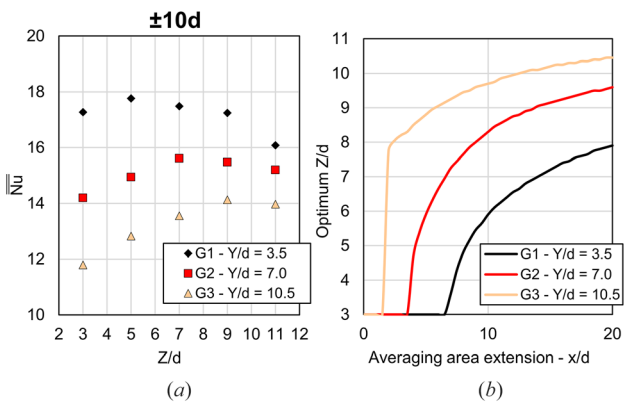

Fig. 14 (*a*) Area-averaged Nu values as a function of *Z/d* and (*b*) optimum *Z/d* value as a function of the averaging area extension for the three geometries—Re = 8000

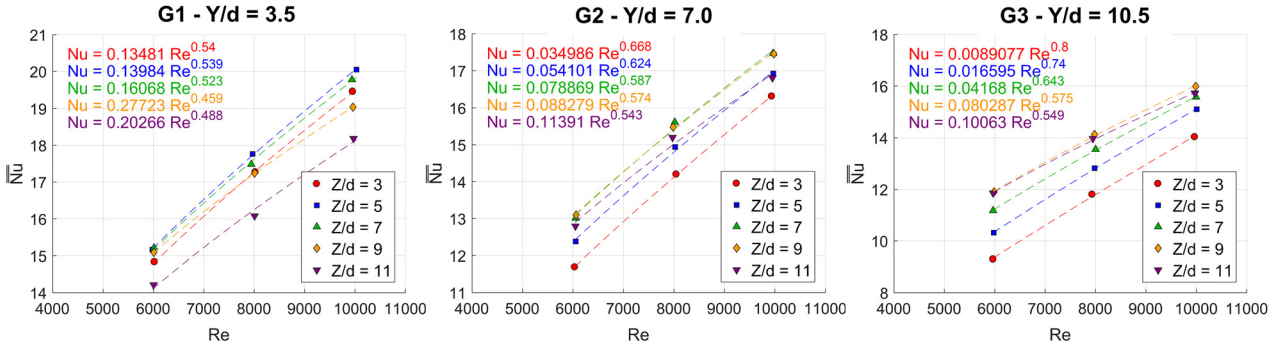

Fig. 15 Area-averaged Nu values ($\pm 10d$ extension) as a function of Re for the three geometries

Re values, which are relatively close to jet transition (expected to occur at around Re = 3000 [4]).

Comparing the three geometries, it can be noted that the exponent of Re increases with jet-to-jet spacing. This can be attributed to the fact that a laminar or transitioning wall flow will exist only up to a certain distance from the jet stagnation point: as a consequence, as jet-to-jet distance increases a smaller fraction of the target wall will experience a laminar flow, thus driving the Re exponent toward larger values.

Effect of Pipe Rotation. In this section, the results obtained when the ACC pipe is rotated around its axis will be presented. As shown in Fig. 16, in this case, rotation is performed so that the geometric stagnation point (i.e., the point where the hole axis crosses the target) moves toward the positive x-direction. With respect to this location, the direction pointing toward the 0 deg stagnation point (i.e., negative x-direction) will be referred to as uphill, while the opposite one (i.e., positive x-direction) will be referred to as downhill, in accordance with literature practice [18].

Figure 17 presents a section of the 2D Nu distributions obtained with geometry G2 ($Y/d = 7.0$) when the ACC pipe is rotated. It can be observed that, as pipe rotation angle α increases, a displacement of the heat transfer peaks toward the direction of pipe rotation occurs, while the magnitude of the peaks progressively decreases. This latter phenomenon can be attributed to both the decrease of jet momentum component normal to the target and to the increase in real jet-to-target distance occurring with rotation, as shown in Fig. 16. If different pipe-to-target distances are considered, it can be noticed that the peak displacement grows with both α and Z/d: this is mostly related to purely geometric effects since as shown in Fig. 16 the spanwise position of the geometric stagnation point is a function of both these values.

The wall jet region also seems to be affected by pipe rotation: while for $\alpha = 0$ deg a clearly symmetric heat transfer pattern is

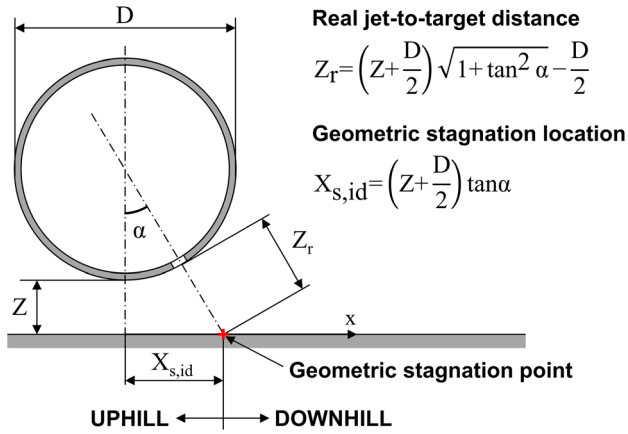

Fig. 16 Scheme of ACC pipe rotation

present surrounding the peaks, as α increases the lateral elongations starting from each peak become longer on the downhill side of the peaks and shorter in the uphill one. In particular, for a given value of α, the elongations on the uphill side seem to almost disappear. Such α value seems to increase with pipe-to-target spacing: at $Z/d = 3$ the uphill elongations tend to disappear at $\alpha = 10$ deg, while this occurs at $\alpha = 20$ deg for $Z/d = 7$ and at $\alpha = 30$ deg for $Z/d = 11$.

Interestingly enough, this latter phenomenon seems to have an effect on cooling performance as well. Considering the line averaged Nu distributions presented in Fig. 18, it can be noticed that a range of pipe rotation angles exists where the peak Nu value is weakly affected, thus generating a sort of plateau-like appearance for the envelope of the peak points. This is a desirable feature, since a range of insensitivity to pipe rotation exists for the cooling performance, making the ACC system highly tolerant to pipe rotational assembly or displacement. The extension of such plateau grows bigger as pipe-to-target distance increases: while for $Z/d = 3$ no plateau seems to be present, for $Z/d = 7$ peaks are very weakly affected by rotation up to $\alpha = 10$ deg and for $Z/d = 11$ up to $\alpha = 20$ deg. Beyond the plateau, peak magnitudes immediately drop to significantly lower values. The comparison of Figs. 17 and 18 reveal that the value of α which identifies the limit of the plateau is very similar to the value corresponding to the disappearance of the elongations on the uphill side of the peaks. Since such elongations are related to the wall jet flow, it can be supposed that at a given pipe rotation angle a change in the wall flow regime occurs: as long as the wall jet is "two-sided" the heat transfer is weakly affected by rotation, while when the wall jet becomes "one-sided" the cooling performance drops.

Figure 18 also reveals that, despite not presenting a real plateau, the heat transfer penalty resulting from pipe rotation is relatively mild at low pipe-to-target distances: for $Z/d = 3$, peak magnitude decreases almost linearly with rotation angle, with a 4% decrease at $\alpha = 5$ deg up to a 26% decrease at $\alpha = 40$ deg. On the opposite side, for $Z/d = 11$ peak values lie within a 5% range up to $\alpha = 20$ deg, but then a sudden decrease of 28% with respect to the 0 deg value occurs at $\alpha = 30$ deg. Area-averaged heat transfer values also reflect the same trends: if a region spanning within $\pm 10d$ from the geometric stagnation point is considered, with $Z/d = 3$ area averaged Nu decreases of 16% passing from 0 deg to 40 deg rotation, while with $Z/d = 11$ the decrease for the same pipe rotation is as large as 32%. As a consequence, even if tolerance to pipe rotation might be increased by using larger pipe-to-target distances, care shall be taken not to have rotation angles exceed the plateau.

All of the previous considerations are true also for the other investigated geometries, i.e., for different jet-to-jet distances: this can be appreciated thanks to Fig. 19, where line averaged Nu distributions are reported for $Z/d = 11$. The only noticeable differences are in the extension of the plateau, which seems to slightly reduce as jet-to-jet distance increases, and in the magnitude of heat transfer drop beyond the plateau, which seems less severe for larger jet-to-jet distances.

Finally, both Figs. 18 and 19 reveal that, as the pipe rotation angle increases, a displacement toward the uphill direction arises

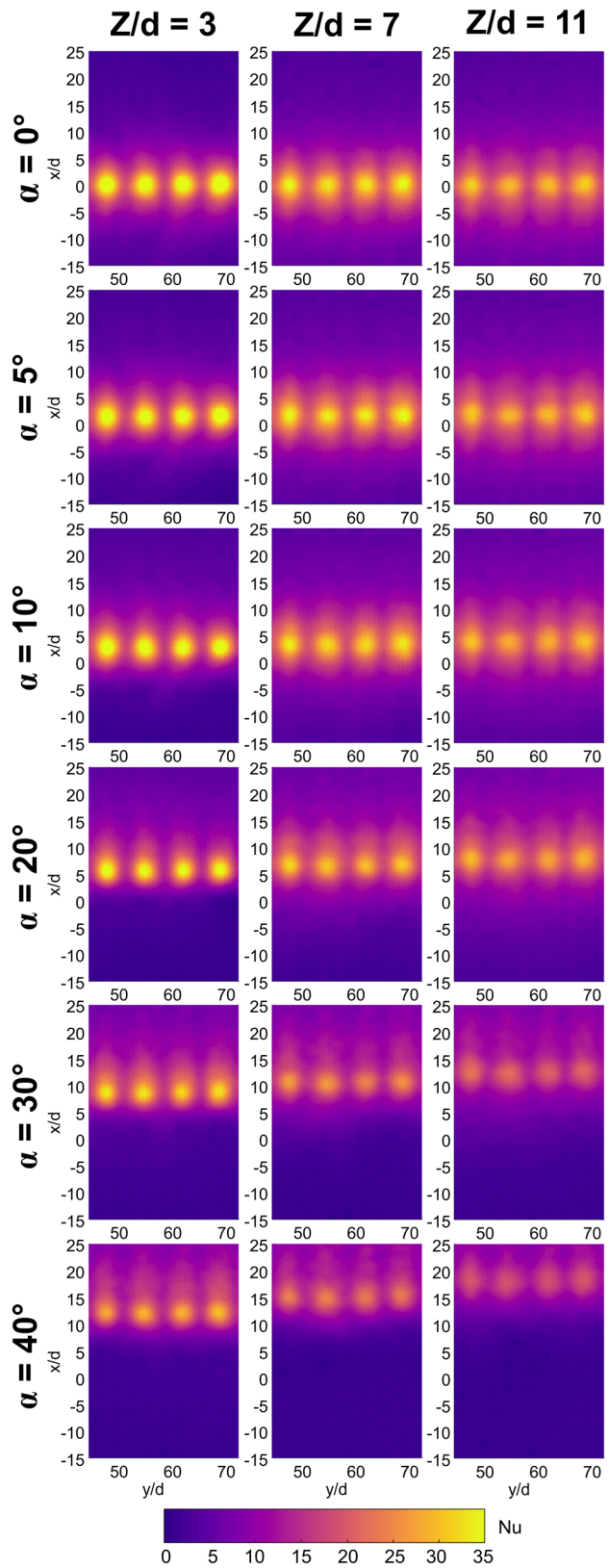

Fig. 17 Pipe rotation effect on 2D Nu distributions—G2 geometry, Re = 8000

between the geometric stagnation point (identified by the dashed lines in the charts) and the peak of heat transfer distribution. Such displacement is a typical feature of oblique impinging jets, even if previous literature studies on this subject focused on a single isolated jet [18–20]. Coherently with the previous investigations, for a given hole pattern the magnitude of the displacement monotonically increases with both pipe rotation angle and pipe-to-target distance (see Fig. 18): in this case, a maximum displacement of 0.7 jet diameters is obtained for $Z/d = 11$ and $\alpha = 40$ deg. Since this work considers a row of impinging jets, a novel finding that the displacement increases as jet-to-jet distance decreases, as shown in Fig. 19: while for the sparsest geometry (G3) the maximum displacement at $\alpha = 40$ deg is $0.5d$, for the densest one (G1) this value is as large as $2.9d$.

Comparison With Literature Data. In order to demonstrate the need for dedicated analysis when dealing with ACC devices, in this section, the outcomes of the present investigation are compared with existing literature data for similar geometries. Various authors pointed out that the available impingement correlations fail in providing reliable results when dealing with ACC systems [8,14]. This is also confirmed in the present case by Fig. 20, where line averaged Nu values obtained from G2 geometry are compared with the prediction of Goldstein and Seol [7] correlation. While close to the stagnation point the correlation provides values around 50% larger than the experimental ones, moving away from this location the predicted values decrease with a slope that is much more intense than the experiment, eventually crossing the measured trend at $x/d \approx 6$. This comparison closely resembles the one reported by Liu et al. [14] and suggests that a significantly different physics is present in the two cases, with a much stronger jet spreading occurring in the present case. In fact, it must be reported that the correlation was retrieved from a row of large scale jets, each fed by an independent pipe: as a consequence, the effects of both the upstream crossflow and the large Mach numbers (related to the large flow velocities) occurring in the present case are expected not to be predicted by the correlation. As a consequence, care shall be taken when applying impingement correlations for the prediction of ACC system performance, and the development of additional knowledge on this kind of device is advisable.

Conclusions

The aim of this work is to characterize the sensitivity of real scale ACC systems to both pipe-to-target distance and pipe rotation, in an attempt to evaluate their cooling performance as well as to quantify the impact of assembly tolerances or geometric thermal deformations. This goal was pursued considering three ACC geometries, presenting a single row of impingement holes arranged with different relative distances. The investigation was carried out with an experimental technique developed and validated in previous work by the same authors, based on steady-state heat transfer measurement and on the solution of inverse heat conduction within the target plate.

The obtained results revealed that the heat transfer patterns obtained for the three geometries are self-similar, i.e., heat transfer values are very close where the local geometry is the same: this suggests that jet-jet interactions are small even for dense hole patterns and large pipe-to-target spacings. The highest cooling performance is obtained with the densest hole pattern, while the most effective coolant exploitation is performed by the sparsest one.

As regards pipe-to-target distance Z, it was found that the effect of this parameter is mainly local: as Z grows, heat transfer decreases close to jet stagnation and increases in the surrounding region. This phenomenon makes the sensitivity to such parameters strongly dependent upon the hole pattern density. It was also revealed that the cooling performance is maximized for a precise pipe-to-target distance, i.e., an optimum value of Z/d exists: such value grows with both jet-to-jet distance and with the extension of the cooled region.

Finally, the analysis of ACC pipe rotation revealed that, while rotation is generally detrimental for heat transfer, a range of

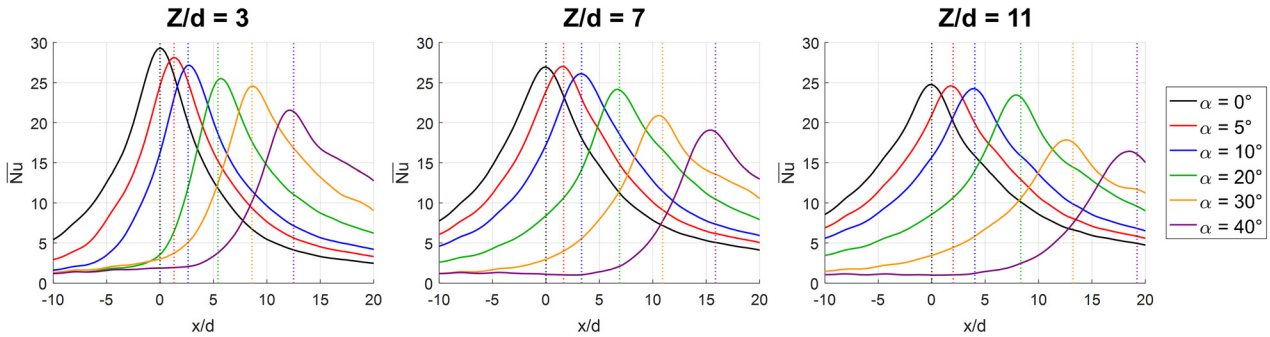

Fig. 18 Pipe rotation effect on line averaged Nu distributions—G2 geometry, Re = 8000

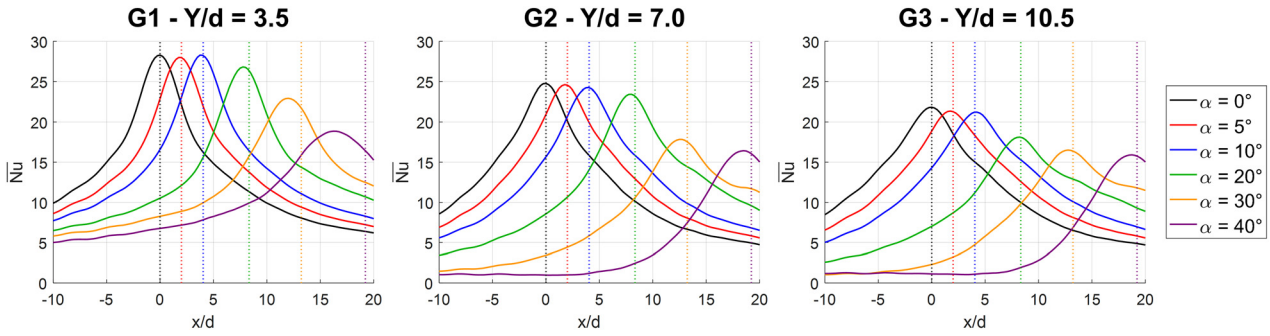

Fig. 19 Pipe rotation effect on line averaged Nu distributions for the three geometries—*Z/d* = 11, Re = 8000

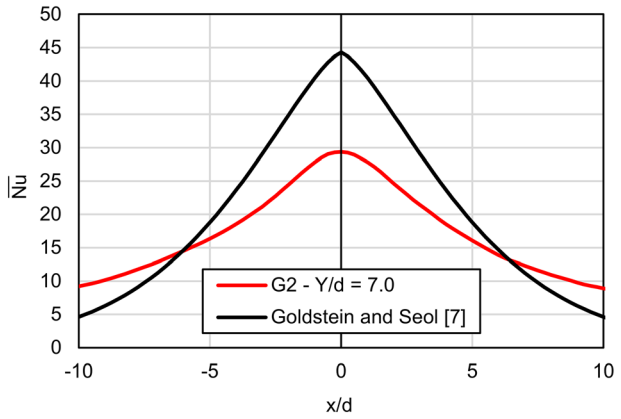

Fig. 20 Comparison between measured and predicted Nu distributions—G2 geometry, *Z/d* = 7, Re = 10,000

insensitivity to such parameter exists where cooling performance is only weakly affected: this is a desirable feature since by exploiting this phenomenon ACC system could be designed to be highly tolerant to pipe rotation. The extension of the insensitivity range increases with pipe-to-target spacing. Even so, a significant drop of cooling performance occurs if pipe rotation grows beyond such range, which is stronger as the range extension is wider: as a consequence, care shall be taken in the design phase so that rotation angle always lies within the insensitivity range. In accordance with the existing literature, it was also found that the peak heat transfer occurs on the uphill side of the geometric stagnation point: the displacement grows with an increase of rotation angle and pipe-to-target distance and with a decrease of jet-to-jet spacing.

The outcomes of this work, once implemented in a design procedure (either as a dataset or as an analytical correlation), could allow to optimize the pipe position in terms of cooling performance, thus reducing the coolant consumption and/or allowing a quicker response for the ACC system. Moreover, the same data could be paired with a thermomechanical model of the engine, in order to obtain a reliable prediction of the mutual interaction between the ACC system displacement and the casing deformation.

Acknowledgment

This activity was carried out in the framework of the project ACCENTO[2] (Active Clearance Control dEsigN and characTerizatiOn), which has received funding from the Clean Sky 2 Joint Undertaking (JU) under grant agreement N° 831815. The JU receives support from the European Union's Horizon 2020 research and innovation program and the Clean Sky 2 JU members other than the Union.

Funding Data

- European Commission (Grant No. 831815; Funder ID: 10.13039/501100000780).

Nomenclature

A = area (m^2)
d = impingement holes diameter (m)
D = manifold diameter (m)
h = convective heat transfer coefficient ($W\ m^{-2}K^{-1}$)
k = air thermal conductivity ($W\ m^{-1}K^{-1}$)
m = mass flow rate ($kg\ s^{-1}$)
N = number of impingement holes
Nu = Nusselt Number
q = heat flux ($W\ m^{-2}$)
R = conductive resistance ($m^2\ K\ W^{-1}$)
Re = Reynolds Number
t = pipe thickness (m)

[2]https://trimis.ec.europa.eu/project/accento-active-clearance-control-design-and-characterization-advanced-investigations

T = static temperature (K)
x = spanwise coordinate (m)
y = streamwise (ACC pipe axis) coordinate (m)
Y = jet-to-jet distance (m)
Z = pipe-to-target distance (m)

Greeks Symbols

α = pipe rotation angle (deg)
ε = emissivity
μ = dynamic viscosity (kg m^{-1} s^{-1})
σ = Stefan-Boltzmann constant (W m^{-2} K^{-4})

Subscripts

ad = adiabatic
amb = ambient
conv = convective
ext = external
int = internal
j = jet
rad = radiative
s = stagnation
tot = overall
w = wall
0 = total

Acronyms

ACC = active clearance control
IR = infrared
LPT = low pressure turbine

References

[1] Arnaldo Valdés, R. M., Burmaoglu, S., Tucci, V., Braga da Costa Campos, L. M., Mattera, L., and Gomez Comendador, V. F., 2019, "Flight Path 2050 and ACARE Goals for Maintaining and Extending Industrial Leadership in Aviation: A Map of the Aviation Technology Space," Sustainability, **11**(7), p. 2065.
[2] Martin, H., 1977, "Heat and Mass Transfer Between Impinging Gas Jets and Solid Surfaces," Adv. Heat Transfer **13**, pp. 1–60.
[3] Viskanta, R., 1993, "Heat Transfer to Impinging Isothermal Gas and Flame Jets," Exp. Therm. Fluid Sci., **6**(2), pp. 111–134.
[4] Zuckerman, N., and Lior, N., '2006, "Jet Impingement Heat Transfer: Physics, Correlations, and Numerical Modeling'," *Advances in Heat Transfer*, G. A. Greene, J. P. Hartnett, A. Bar-Cohen, and Y. I. Cho, eds., Vol. 39, Elsevier, Amsterdam, The Netherlands, pp. 565–631.
[5] Soghe, R. D., and Andreini, A., 2013, "Numerical Characterization of Pressure Drop Across the Manifold of Turbine Casing Cooling System," ASME J. Turbomach., **135**(3), p. 031017.
[6] Andreini, A., and Soghe, R. D., 2012, "Numerical Characterization of Aerodynamic Losses of Jet Arrays for Gas Turbine Applications," ASME J. Eng. Gas Turbines Power, **134**(5), pp. 921–929.
[7] Goldstein, R., and Seol, W., 1991, "Heat Transfer to a Row of Impinging Circular Air Jets Including the Effect of Entrainment," Int. J. Heat Mass Transfer, **34**(8), pp. 2133–2147.
[8] Ben Ahmed, F., Weigand, B., and Meier, K., 2011, "Heat Transfer and Pressure Drop Characteristics for a Turbine Casing Impingement Cooling System," ASME Paper No. IHTC14-22817.
[9] Ben Ahmed, F., Tucholke, R., Weigand, B., and Meier, K., 2012, "Numerical Investigation of Heat Transfer and Pressure Drop Characteristics for Different Hole Geometries of a Turbine Casing Impingement Cooling System," ASME Paper No. GT2011-45251.
[10] Ben Ahmed, F., Poser, R., Schumann, Y., von Wolfersdorf, J., Weigand, B., and Meier, K., 2012, "A Numerical and Experimental Investigation of an Impingement Cooling System for an Active Clearance Control System of a Low Pressure Turbine," ISROMAC 2012—14th International Symposium Transportation Phenomenon Dynamic Rotating Machine, Honolulu, HI, Feb. 27–Mar. 2.
[11] Marzec, K., and Kucaba-Pietal, A., 2014, "Heat Transfer Characteristics of an Impingement Cooling System With Different Nozzle Geometry," J. Phys. Conf. Series, **530**, p. 012038.
[12] Choi, M., Dyrda, D. M., Gillespie, D. R. H., Tapanlis, O., and Lewis, L. V., 2016, "The Relative Performance of External Casing Impingement Cooling Arrangements for Thermal Control of Blade Tip Clearance," ASME J. Turbomach., **138**(3), p. 031005.
[13] Liu, F., Mao, J., Han, X., and Gu, W., 2018, "Heat Transfer of Impinging Jet Arrays on a Ribbed Surface," J. Thermophys. Heat Transfer, **32**(3), pp. 669–679.
[14] Liu, F., Mao, J., Han, C., Liu, Y., Han, X., and Liang, F., 2019, "Study of a Cooling Feed Pipe With a Covering Plate on a Ribbed Turbine Case," ASME J. Eng. Gas Turbines Power, **141**(7), p. 071024.
[15] Andreini, A., DaSoghe, R., Facchini, B., Maiuolo, F., Tarchi, L., and Coutandin, D., 2013, "Experimental and Numerical Analysis of Multiple Impingement Jet Arrays for an Active Clearance Control System," ASME J. Turbomach., **135**(3), p. 031016.
[16] Da Soghe, R., and Bianchini, C., 2019, "Aero-Thermal Investigation of Convective and Radiative Heat Transfer on Active Clearance Control Manifolds," ASME Paper No. GT2019-90007.
[17] Soghe, R. D., Bianchini, C., Andreini, A., Facchini, B., and Mazzei, L., 2016, "Heat Transfer Augmentation Due to Coolant Extraction on the Cold Side of Active Clearance Control Manifolds," ASME J. Eng. Gas Turbines Power, **138**(2), p. 021507.
[18] Sparrow, E. M., and Lovell, B. J., 1980, "Heat Transfer Characteristics of an Obliquely Impinging Circular Jet," ASME J. Heat Transfer-Trans. ASME, **102**(2), pp. 202–209.
[19] Goldstein, R. J., and Franchett, M. E., 1988, "Heat Transfer From a Flat Surface to an Oblique Impinging Jet," ASME J. Heat Transfer-Trans. ASME, **110**(1), pp. 84–90.
[20] Yan, X., and Saniei, N., 1997, "Heat Transfer From an Obliquely Impinging Circular, Air Jet to a Flat Plate," Int. J. Heat Fluid Flow, **18**(6), pp. 591–599.
[21] Da Soghe, R., Mazzei, L., Tarchi, L., Cocchi, L, Picchi, A., Facchini, B., Descamps, L., Girardeau, J., and Simon, M., 2020, "Development of Experimental and Numerical Methods for the Analysis of Active Clearance Control Systems," ASME J. Eng. Gas Turbines Power, **143**(2), p. 021018.
[22] Bouchez, J.-P., and Goldstein, R. J., 1975, "Impingement Cooling From a Circular Jet in a Cross Flow," Int. J. Heat Mass Transfer, **18**(6), pp. 719–730.
[23] Attalla, M., and Specht, E., 2009, "Heat Transfer Characteristics From in-Line Arrays of Free Impinging Jets," Heat Mass Transfer, **45**(5), pp. 537–543.
[24] Goodro, M., Park, J., Ligrani, P. M., Fox, M., and Moon, H.-K., 2007, "Effects of Mach Number and Reynolds Number on Jet Array Impingement Heat Transfer," Int. J. Heat Mass Transfer, **50**(1–2), pp. 367–380.
[25] Fenot, M., Vullierme, J.-J., and Dorignac, E., 2005, "Local Heat Transfer Due to Several Configurations of Circular Air Jets Impinging on a Flat Plate With and Without Semi-Confinement," Int. J. Therm. Sci., **44**(7), pp. 665–675.
[26] Bergman, T. L., Incropera, F. P., DeWitt, D. P., and Lavine, A. S., 2011, *Fundamentals of Heat and Mass Transfer*, Wiley, Hoboken, NJ.
[27] Bozzoli, F., Cattani, L., Rainieri, S., Viloche Bazán, F. S., and Borges, L. S., 2014, "Estimation of the Local Heat-Transfer Coefficient in the Laminar Flow Regime in Coiled Tubes by the Tikhonov Regularisation Method," Int. J. Heat Mass Transfer, **72**, pp. 352–361.
[28] Rubinstein, R. Y., and Kroese, D. P., 2016, *Simulation and the Monte Carlo Method*, Wiley, Hoboken, NJ.
[29] ASME, 1985, "Measurement Uncertainty," Instrum. Appar., Vol. ANSI/ASME PTC 19.1-1985 of Performance Test Code, ASME, New York.
[30] Kline, S. J., and McClintock, F. A., 1953, "Describing Uncertainties in Single Sample Experiments," Mech. Eng., **75**, pp. 3–8.
[31] Goldstein, R. J., Behbahani, A. I., and Heppelmann, K. K., 1986, "Streamwise Distribution of the Recovery Factor and the Local Heat Transfer Coefficient to an Impinging Circular Air Jet," Int. J. Heat Mass Transfer, **29**(8), pp. 1227–1235.